13. Territo, P. R., Heil, J., Bose, S., Evans, F. J. and Balaban, R. S., Fluorescence absorbance inner-filter decomposition: the role of emission shape on estimates of free Ca^{2+} using Rhod-2. *Appl. Spectrosc.*, 2007, **61**, 138–147.

14. Iasilli, G. *et al.*, Aggregation-induced emission of tetra-phenylethylene in styrene-based polymers. *Macromol. Chem. Phys.*, 2014, **215**, 499–506.

15. Lagorio, M. G. and San Romn, E., How does light scattering affect luminescence? Fluorescence spectra and quantum yields in the solid phase. *J. Chem. Educ.*, 2002, **79**, 1362–1367.

16. Maar, R. R. and Gilroy, J. B., Aggregation-induced emission enhancement in boron difluoride complexes of 3-cyanoformazanates. *J. Mater. Chem. C*, 2016, **4**, 6478–6482.

17. Singh, R. S. *et al.*, Morphological tuning via structural modulations in AIE luminogens with the minimum number of possible variables and their use in live cell imaging. *Chem. Commun.*, 2015, **51**, 9125–9128.

18. Srivastava, A. K. *et al.*, Pyridyl substituted 4-(1,3-dioxo-1H,3H-benzo[de]isoquinolin-2-ylmethyl)-benzamides with aggregation enhanced emission and multi-stimuli-responsive properties. *J. Lumin.*, 2017, **182**, 274–282.

19. Feng, Q., Wang, M., Dong, B., Xu, C., Zhao, J. and Zhang, H., Tuning solid-state fluorescence of pyrene derivatives via a cocrystal strategy. *CrystEngComm*, 2013, **15**, 3623.

20. Khan, T. and Datta, A., Enhanced fluorescence with nanosecond dynamics in the solid state of metal ion complexes of alkoxy salophens. *Phys. Chem. Chem. Phys.*, 2017, **19**, 30120–30127.

21. Birks, J. B., *Photophysics of Aromatic Molecules*, Wiley-Interscience, London, 1970, 2nd edn.

22. Prunty, S. L., The effect of absorption on the quantum efficiency and decay-time in organic scintillators. *Nucl. Instrum. Methods Phys. Res., Sect.*, 1986, **245**, 563–565.

23. Birks, J. B. and Wright, G. T., Fluorescence spectra of organic crystals. *Proc. Phys. Soc. Sect. B*, 1954, **67**, 657–663.

24. Khan, T., Vaidya, S., Mhatre, D. S. and Datta, A., The prospect of salophen in fluorescence lifetime sensing of Al^{3+}. *J. Phys. Chem. B*, 2016, **120**, 10319–10326.

25. Khan, T. and Datta, A., Impact of molecular arrangement and torsional motion on the fluorescence of salophen and its metal complexes. *J. Phys. Chem. C*, 2017, **121**, 2410–2417.

26. Leese, R. A. and Wehry, E. L., Corrections for inner-filter effects in fluorescence quenching measurements via right-angle and front-surface illumination. *Anal. Chem.*, 1978, **50**, 1193–1197.

27. Ventura, B. *et al.*, Luminescence Properties of 1,8-naphthalimide derivatives in solution, in their crystals and in co-crystals: toward room-temperature phosphorescence from organic materials. *J. Phys. Chem. C*, 2014, **118**, 18646–18658.

28. Kirgan, R. A., Witek, P. A., Moore, C. and Rillema, D. P., Physical, photophysical and structural properties of ruthenium(ii) complexes containing a tetradentate bipyridine ligand. *Dalton Trans.*, 2008, 3189.

Asp72 of pro-peptide is an important pH sensor in the zymogen activation process of papain: a structural and mechanistic insight

Sumana Roy[1] and Sampa Biswas[1,2,*]

[1]Crystallography and Molecular Biology Division, Saha Institute of Nuclear Physics, 1/AF Bidhannagar, Kolkata 700 064, India
[2]Homi Bhabha National Institute, Anushakthinagar, Mumbai 400 094, India

The zymogen of papain contains a pro-peptide at the N-terminus of the catalytic domain. Pro-peptide contains residues which act as pH-sensors in zymogen activation cascade. To understand the influence of pro-peptide in the pH-induced zymogen activation process of the protease, we performed structural studies of the zymogen of papain at activation pH of 4.0. The X-ray structure of zymogen at acidic pH reveals that Asp72 of the pro-peptide, a highly conserved residue of the GXNXFX**D** motif, plays an important role in pH-induced conformational changes in the pro-domain leading to the zymogen activation process. Far-UV circular dichroism spectrum of zymogen at pH 4.0 demonstrates loss of helical structure compared to that at pH 8.0. The structural observation is further corroborated by mutational studies, where D72A mutant is shown to undergo auto-activation at pH 5.0 compared to pH 4.0 for wild-type, though the general proteolytic activity of the D72A mutant remains similar to that of wild-type. Our findings indicate that the conserved Asp72 residue is an important pH sensor in the zymogen activation process and that the pro-peptide part can also be a useful target of protein engineering for altering the activation pH of a protease.

PAPAIN (EC 3.4.22.2), a cysteine protease from the tropical plant *Carica papaya*, has considerable commercial significance because of its wide uses in various industrial processes[1]. It also has different medical applications like in gastric fermentation, gastritis, to assist protein digestion in chronic dyspepsia, preparation of tyrosine derivatives for the treatment of Parkinsonism, removal of necrotic tissue, preparation of tetanus vaccines, cleansing agents of skin, treatments of acne, etc.[2]. Papain has been characterized extensively from the kinetic, molecular and structural point of view[3,4]. It is the first proteolytic enzyme whose crystal structure was determined in 1968 (ref. 5). Papain, the archetype enzyme of papain-like cysteine proteases (clan C1A) shares a common fold with other members of the family having a molecular weight

*For correspondence. (e-mail: sampa.biswas@saha.ac.in)

of ~21–30 kDa (ref. 6). The mature catalytic domains of papain-like proteases are folded into two compact interacting domains of comparable size (Figure 1), delimiting a cleft with active site residues cysteine and histidine, forming the zwitterionic catalytic dyad (Cys⁻...His⁺)[7].

Papain-like cysteine proteases are generally synthesized as a precursor protein in the cell with a pre-peptide, a pro-segment and a mature catalytic domain. The pre- or signal-peptide is required for translocation of the enzyme and is cleaved-off by the signal peptidases after transportation[8]. The pro-segment works as an intramolecular chaperone that acts as a foldase in folding of the catalytic domain of the cognate protease[8,9]. Apart from its chaperone activity, pro-segment also blocks the catalytic cleft in the zymogenic form and renders the enzyme in a catalytically latent condition[10]. This spacio-temporal regulation of proteolytic activity is maintained by the N-terminal pro-segment for papain-like cysteine protease[8–10]. The N-terminal part of the pro-segment generally forms a domain called the pro-domain consisting of three α-helices and a short β-strand and the rest of the pro-segment is in an extended conformation (Figure 1). A part of this extended pro-segment blocks the active site cleft by positioning itself in the reverse direction of a natural substrate (non-productive orientation), thus preventing access of substrates to the catalytic site of the protease[11]. The pro-domain works as a scaffold that helps in positioning the extended part to block the catalytic cleft[11]. Comparing the structures of the zymogens of the family[12–16], it is reported that binding of the pro-segment is mediated by interactions in two key areas of the catalytic domain: one is at the pro-segment binding loop (PBL) of the right domain of the mature protease part (or catalytic domain) and the other is at the substrate-binding sub-sites of the catalytic domain (Figure 1). The shortest helix of pro-domain interacts with primed subsites and a part of the extended pro-peptide passes through unprimed subsites of the catalytic cleft.

It has been already established that the pro-domain contains the key(s) for pH-dependent activation process[9–11]. Our earlier studies showed that zymogen activation of papain generally occurs at acidic pH in a stepwise manner[16]. Structures of different zymogens of the papain-family reveal that at near-neutral pH, some highly conserved aspartic acid and glutamic acid residues of the pro-peptide are involved in making H-bonds/salt-bridges, and thus stabilize the scaffolding domain of zymogen structures[12–16]. At acidic pH, due to protonation of glutamic acid and aspartic acid residues, these H-bonds/salt-bridges are expected to be altered or disrupted. The structural loosening of the pro-domain at lower pH destabilizes the interface between the pro-domain and the catalytic domain of zymogen to a large extent and thereby triggers the activation process. However, zymogen activation mechanism is not yet fully explored at the molecular level. This study presents a structure of zymogen of papain at

its activation pH. A structural comparison of the low pH and near-neutral pH structures along with biophysical characterization reveals the functional role of aspartic acid and glutamic acid residues of pro-peptide in the zymogen activation process. Subsequent mutation of Asp72 to Ala72 further establishes the fact.

In an earlier study, we have generated a thermostable mutant of papain which retains all the catalytic properties of wild-type papain[17]. We also solved the structure of this thermostable papain at neutral pH (ref. 16). This mutant of papain has been chosen as a model system to understand the pH-sensing mechanism in papain-like proteases. Crystals of this thermostable pro-papain were grown as described before[18] for neutral pH structure. These crystals were transferred to a 4 µl drop of 0.1 M Na-acetate buffer, pH 4.0 with 8% PEG 3350 and equilibrated overnight against reservoir solution for soaking at low pH. The soaked crystals were cryo-protected with soaking solution supplemented with 30% glycerol before freezing for data collection.

X-ray diffraction datasets were collected at BM14 beamline, European Synchrotron Radiation Facility (ESRF), Grenoble, France, on a Mar-CCD detector at 100 K from flashed cooled crystals. The diffraction data were processed and scaled using HKL2000 program[19]. Molecular replacement was performed with PHASER[20] in PHENIX[21] using neutral-pH structure (PDB ID: 3TNX) as a model. Iterative rounds of model-building with COOT[22] and refinement using PHENIX[21] and REFMAC5[23] were performed using a translation–liberation–screw model of the atomic displacement parameters. The stereochemistry of the final model of the structure was checked using PROCHECK[24]. Coordinates and structure factors were deposited in the protein Data Bank with accession code 4QRX (PDB ID: 4QRX). Table 1 shows the diffraction data statistics and refinement data.
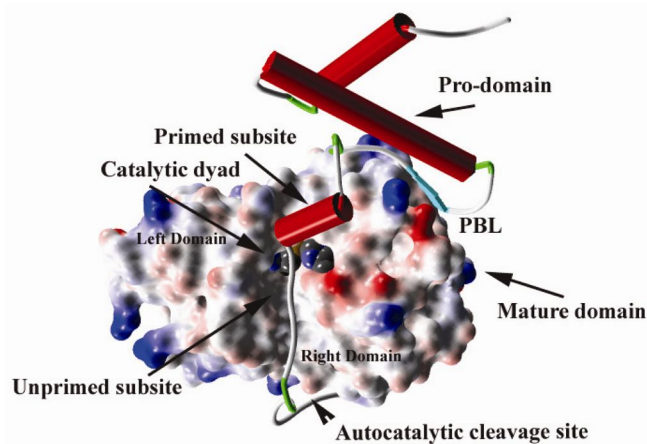
Figure 1. Three-dimensional structure of zymogen of papain (PDB ID: 3TNX); catalytic domain is represented as electrostatic potential surface with catalytic dyad residues depicted as CPK model. The pro-peptide is depicted in ribbon.

In the present study, cDNA of the thermostable mutant of pro-papain, cloned in pET30 Ek/LIC vector[17], was used to introduce D72A mutant. The expression and purification of D72A thermostable pro-papain were done using the same protocol described earlier for wild-type papain[17]. Standard protocols outlined in the QuickChange Site-Directed Mutagenesis Kit (Agilent Technologies, Inc., USA) were used for mutagenesis. Forward and reverse primers used for PCR mutagenesis are 5′GGATTAAA-TGTGTTTGCT<u>GCG</u>ATGAGCAATGATGAATTC3′ and 5′GAATTCATCATTGCTCAT<u>CGC</u>AGCAAACACATT-TAATCC 3′.

Zymography was done in 12% SDS–PAGE co-polymerized with 0.1% gelatin as a substrate, following the protocol described by Choudhury *et al.*[25]. Clear zones on a light-blue background after coomassie staining indicated active protease bands.

Activation of pro-proteases of wild-type and D72A mutant was monitored in different values of pH, temperature and at different time periods of incubation. For activation at different pH values, pro-proteases were adjusted to the desired pH (4.0 and 5.0) with 100 mM sodium acetate buffer containing 20 mM cysteine as activator and 5 mM EDTA, and incubated for different time-periods at

Table 1. Data collection and refinement statistics

PDB code	4QRX
Data statistics	
Beamline	BM14, ESRF
Wavelength (Å)	0.97
Resolution range (Å)	40.52–3.138 (3.25–3.138)
Space group	P 1 21 1
Unit cell (a, b, c in Å and β in °)	42.59, 74.21, 116.23 and 92.46
Total reflections	37,450
Unique reflections	12,482 (1127)
Multiplicity	3.0 (2.8)
Completeness (%)	97.40 (89.23)
Mean $I/\sigma(I)$	9.30 (2.08)
Wilson B-factor (Å^2)	56.84
R-merge	0.075 (0.37)
Refinement statistics	
R-work	0.1622 (0.2152)
R-free	0.2544 (0.3172)
Number of non-hydrogen atoms	4855
Protein	4782
Water	73
Protein residues	599
RMS (bonds, Å)	0.010
RMS (angles, °)	1.43
Ramachandran favoured (%)	85
Ramachandran outliers (%)	4.2
Average B-factor (Å^2)	62.30
Protein	62.50
Solvent	46.00

Statistics for the highest resolution shell is shown in parenthesis. R-merge = SUM$((I - \langle I \rangle)^2)$/SUM$(I^2)$. R-work = $\sum F_o - F_c/\sum F_o$. R-free is the cross-validation R factor for the test set (5%) of reflections omitted in model refinement.

two activation temperatures (40°C and 50°C). The reaction was terminated by the addition of irreversible inhibitor E-64. Progress of activation process and generation of cognate mature proteases were monitored by running the samples in 15% SDS–PAGE.

Far-UV circular dichroism (CD) spectra were measured using a circular dichroism spectrophotometer (Jasco, Inc. Jasco J-815). Ellipticity at pH 8.0 and 4.0 was measured by diluting a stock solution of ~2 mg/ml protein in 10 mM Tris buffer, pH 8.0 with 1% glycerol and 10 mM NaCl to ~30 μg/ml in the same buffer, and in 100 mM Na-acetate buffer, pH 4.0 with 1% glycerol and 10 mM NaCl respectively. The protein was incubated for 10 min at room temperature in pH 4.0 buffer prior to CD experiment. Measurements were made in triplicate with 1 nm steps using a quartz cuvette of 0.1 cm path length. Spectra were recorded between 200 and 260 nm at a speed of 100 nm/5 min. The secondary structures were predicted using the K2D program from DichroWeb[26].

Our attempts to grow crystals of active-site cysteine knock-out papain (C132A) at the activation pH of papain (pH 4.0) were not successful. This may be due to conformational disorder of the pro-domain at this pH. Therefore we soaked a crystal, grown in neutral pH as described earlier[18], in an acidic buffer of pH 4.0 overnight and were able to get 3.15 Å data from the crystal. However, absolute pH value inside the crystal could not be conclusively defined. The soaked crystal had the same space group and similar unit cell parameters (Table 1) like those of a crystal grown at neutral pH[18]. It is therefore true that due to crystal packing constraint, total conformational change(s) at this pH may not have taken place, but this low pH structure demonstrates some important information regarding the initiation or onset of pH-induced conformational changes which trigger the activation process. Two molecules in the asymmetric unit are found for both the crystal structures at different pH values. Whereas in the neutral pH structure both molecules of the asymmetric unit are similar[16], in the low pH structure the second molecule of the asymmetric unit differs from the first as well as from two molecules of the neutral pH structure. Moreover, in the second molecule of the low-pH structure, the entire pro-peptide backbone atoms could be traced from the electron density map. Therefore, all discussions on the pH-induced conformational changes were made based on this second molecule. As the structure at pH 4.0 is based on a comparatively low-resolution dataset and electron densities of side chain of some residues were not clear, we presumed that these residues are disordered due to loss of stabilizing interaction(s) at low pH. In the neutral pH structure of zymogen (PDB ID: 3TNX), it was observed that the scaffold of pro-domain is stabilized by two clusters of integrated salt-bridge/H-bond network (Figure 2 *a*)[16]. Three helices of the pro-domain, i.e. H1, H2 and H3, are stabilized by salt-bridge/H-bonds involving three acidic residues, i.e.

Figure 2. Comparison of neutral pH and low pH structures of the pro-domain region. **a**, Neutral pH structure (taken from PDB ID: 3TNX). **b**, Same region of the structure at acidic pH. **c**, The thin bonds are for atoms which do not have well-defined electron density at 1.0σ level in 2mFo-DFc map. **d** and **e**, Superposition of neutral pH (purple) and low pH (sky blue) structures around residues E55 and E242 of pro- and mature catalytic domain respectively. Black lines indicate H-bond/salt-bridge interactions.

Asp72, Glu38 and Glu77 respectively, with their neighbouring residues (Figure 2 *a*). These amino acid side-chains are expected to be in their charged deprotonated condition at neutral pH. Asp72 is the central residue in one of the clusters and stabilizes the H1–H2 inter-helical loop. The side-chain atoms OD1 and OD2 of Asp72 form resonating bifurcated H-bond with OH atom of Tyr33. OD2 is also involved in the formation of H-bond with Lys31; both Tyr33 and Lys31 are from the inter-helical loop. In the corresponding region in the low-pH structure, we observed important changes in this network. The bifurcated interaction between Tyr33 and Asp72 was lost, while Asp72 side-chain reoriented to make a single H-bond with Tyr33-OH atom. The interaction with Lys31 was presumed to be absent (Figure 2 *b*), as there was no well-defined density for the side-chain of Lys31 (Figure 2 *c*). The calculated pKa values of Asp72 at pH 4.0 are around 4.5 (http://propka.ki.ku.dk/). Therefore, these changes in the interactions are due to protonation of Asp72 at pH 4.0. Removal of two salt-bridges/H-bond of Asp72 weakens the bridging interaction with H1–H2 inter-helical loop, which may facilitate a scaffold loosening of the pro-domain. Another cluster of H-bond/salt-bridge network was formed by residues Glu38, Arg42 and Glu77, with Arg42 at the centre and this network stabilizes the helices H2, H3 and the connecting loop region

(Figure 2 *a*). The pKa value of Glu38 was around 5.0 in the low-pH structure and therefore protonation of Glu38 at pH 4.0 may be responsible for loosening the salt-bridges/H-bond network with Arg42 (Figure 2 *b*) in this region, leading to further destabilization of the structure in this region. It is known that highly acidic condition of lysozomes is instrumental for *in vivo* activation of lysozomal papain-like cysteine proteases[27]. Vernet *et al.*[28] also demonstrated that mutation of Asp72 can make the zymogen structure unstable and latency of the protease at neutral pH is not maintained[27]. Among the three residues, viz. Asp72, Glu38 and Glu77, Asp72 is highly conserved in the papain family and is a part of the conserved motif GNF<u>D</u>. On the other hand, Glu38 and Glu77 are involved in making H-bond/salt-bridges with Arg42, a residue of the motif <u>E</u>RFNIN. Glu55 of helix H2 of the pro-domain and Glu242 of the mature domain also show loss of H-bond/salt-bridge interactions with their neighbouring residues in low-pH structure (Figure 2 *d* and *e*). Loss of interaction of Glu55 side-chain causes distortion of helix H2 (Figures 2 *d* and 3 *a*). On the other hand, in the mature domain no such significant backbone alteration is observed in and around Glu242. Papain and most of the papain-like proteases have pH optima of activity in the acidic range and inactive zymogenic form is stable at basic pH. Glu242 is a conserved residue in the papain

family and is at the proximity of catalytic His266. Therefore, loss of interaction of this region at low pH may generate the necessary flexibility required for dynamic movement of catalytic cleft during catalysis.

The B-factor plot of the low-pH structure indicates higher thermal vibration in the pro-domain compared to neutral pH structure (Figure 3 b). In contrast, B-factor plot shows that mature catalytic domain (residues 108–319) attains lower or comparable B-values at acidic pH, which corroborates the established fact that low-pH destabilizes the pro-domain without any significant alteration in the catalytic domain and makes auto-catalytic activation possible. However, total structural changes at

acidic pH may not have been attained due to crystal packing constraints. So to understand the effect of pH on the secondary structure in solution, we performed far-UV CD experiment of C132A, which revealed significant loss of secondary structural element(s) mainly in helical structures at pH 4.0 compared to those at pH 8.0 (from 26% to 16%) (Figure 3 c). Even though there is a decrease in spectral intensity at 208 and 222 nm at pH 4.0 (corresponding to the decrease in helicity), the negative to positive cross-over points did not alter much, indicating that a part of the secondary structure remained unaltered at pH 4.0, which is likely to be the mature catalytic domain part of zymogen. The percentage of helical structure calculated from the X-ray structure of zymogen of papain (PDB ID: 3TNX) at neutral pH is 27.2 (considering the uncleaved His tag part of the protein), and this corroborates our observation from far-UV CD studies at pH 8.0. The contribution of the three helices in the pro-peptide is almost 11.8% in this structure (PDB ID: 3TNX). Therefore if these three helices become disordered, the expected
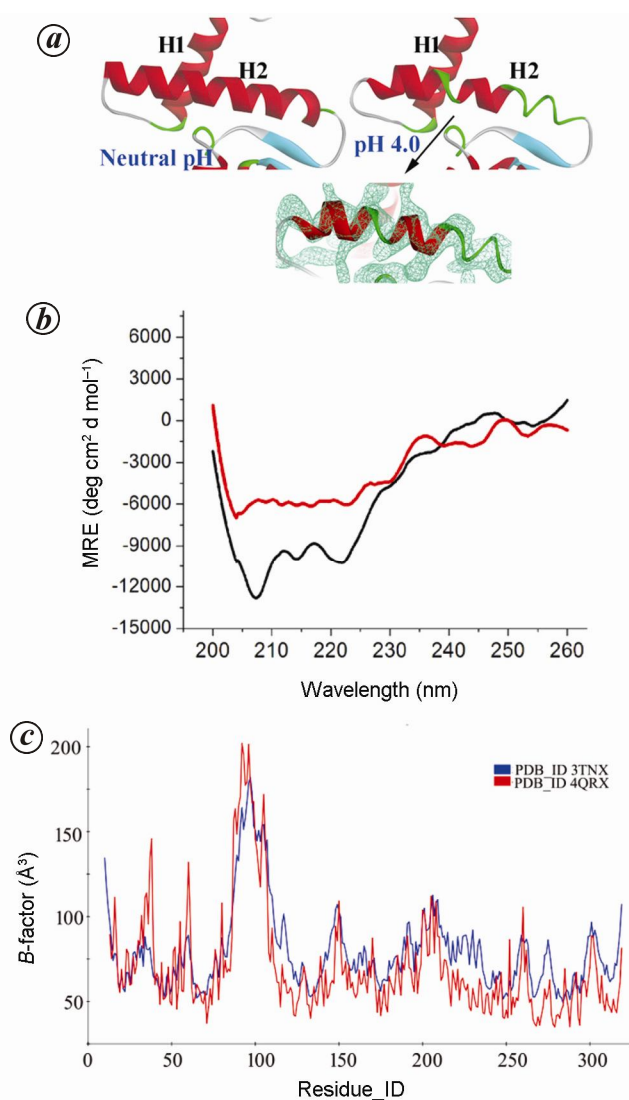
Figure 3. Comparison of secondary structural elements in the pro-domain. a, Helices H1 and H2 of pro-domain at neutral (taken from PDB ID: 3TNX) and low pH structures. 2 m F_o–DF_c electron density map contoured at 1.2σ level associated with the backbone of helix H2 of pH 4.0 structure is shown below. b, Far-UV circular dichroism of pro-papain at pH 8.0 (black) and pH 4.0 (red). c, B-factor plot of neutral pH structure (PDB ID: 3TNX) and structure at acidic pH.
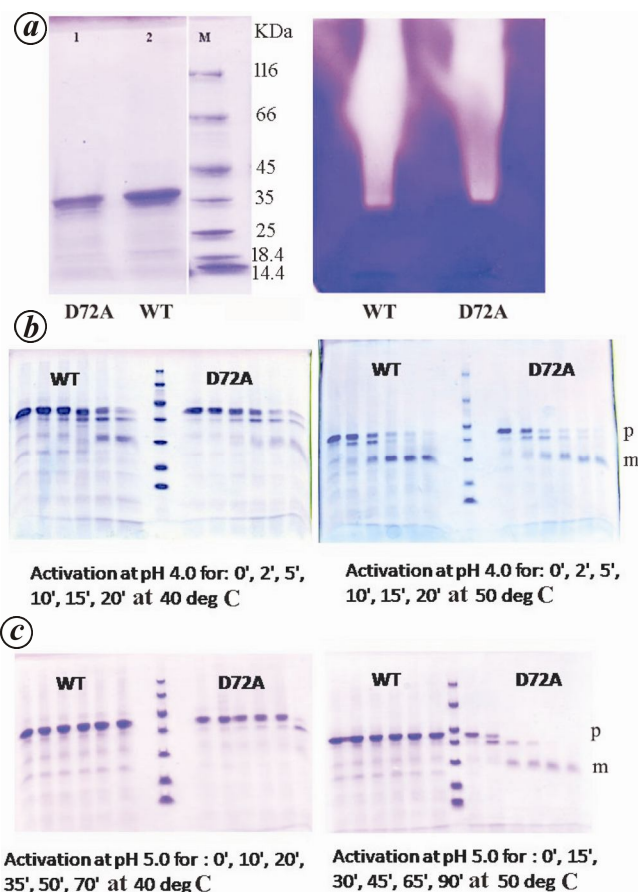
Figure 4. SDS–PAGE analyses of the proteases. a, Purified pro-proteases. b, Gelatin gel zymography with 8 μg pro-proteases. c, Comparison of zymogen activation profile of papain D72A mutant and wild-type: variable parameters of activation are mentioned below the images. Same molecular weight marker protein was used as shown in (a). p and m denote position of pro- and mature form of the protease respectively.

helicity will become 15.4% in the three-dimensional structure of zymogen, which again matches the value (16%) observed from its far-UV CD spectra at pH 4.0. Thus, one can conclude that the pro-domain loses its structural integrity at low pH, which probably leads to dissociation of the pro-part from the catalytic domain and accessibility of the catalytic cleft is increased, which triggers the activation process.

In order to understand the role of aspartic acid residue of GNF**D** motif, we mutated the residue of pro-papain by an alanine residue. The heterologous expression level and yield of the pure mutant protein are comparable to its wild-type counterpart (Figure 4 *a*). The gelatin zymography also shows that the proteolytic activity of the mutant is similar to that of wild-type (Figure 4 *b*).

Zymogen activation of D72A mutant was investigated as a function of pH, temperature and time, and the activation kinetics was compared with wild-type papain. *In vitro* activation of wild-type papain generally occurs by incubating the pro-papain at 50°C in a buffer pH 4.0 for 20–30 min[25]. Activation is also possible at 40°C at a slower rate. For both temperatures, alterations of activation kinetics for the mutant D72A are not significant (Figure 4 *c*). However, at pH 5.0, we observed that the activation process of mutant D72A was substantially faster compared to wild-type papain at 50°C and 40°C (Figure 4 *c*). Wild-type pro-papain did not get activated at pH 5.0, even after incubation at 50°C for 90 min. On the other hand, the mutant started its activation after 15 min of incubation at the same pH and temperature (Figure 4 *c*). This observation indicates that Asp72 of pro-peptide of papain, a conserved residue in the papain family, is an important pH sensor of papain and most likely other members of the family as well.

Our studies demonstrate the importance of the well-tuned H-bond/salt-bridges network of the pro-domain, the key regulator of pH-dependent activation process of papain-like cysteine proteases. These networks are observed at the core of the pro-domain scaffold and not at the pro-mature interface. The integrity of these networks is lost due to changes in protonation status of the constituting residues at activation pH (acidic pH), leading to a structural loosening of the scaffold of the pro-domain. The association affinity towards the mature domain may reduce due to this structural loosening. At higher pH, above the pH optima of activation, the stable and compact form of the pro-domain is responsible for its association with the mature domain and renders the enzyme in a latent state. Our studies show that Asp72 is an important residue in this pH sensing network.

This study shows that by judicially identifying residues responsible for pH-sensing of auto-activation process in the pro-domain, one can design and generate proteases with tailor-made activation pH with minimal alteration in the proteolytic activity for a protease of the papain family having medical and biotechnological relevance.

1. Rawlings, N. D. and Barrett, A. J., Families of cysteine peptidases. *Meth. Enzymol.*, 1994, **244**, 461–486.
2. Grzonka, Z., Kasprzykowski, F. and Wiczk, W., In *Industrial Enzymes: Structure, Function and Applications* (eds Polaina, J. and MacCabe, A. P.), Springer, The Netherlands, 2007, pp. 181–195.
3. Baker, E. N. and Drenth, J., In *The Thiol Proteases: Structure and Mechanism in Biological Macromolecules and Assemblies* (eds Jurnak, F. A. and McPherson, A.), Wiley, New York, USA, 1987, pp. 313–368.
4. Polgár, L., In *Mechanisms of Protease Action*, CRC Press, Boca Raton, FL, USA, 1989, pp. 43–76.
5. Drenth, J., Jansonius, J. N., Koekoek, R., Swen, H. M. and Wolthers, B. G., Structure of papain. *Nature*, 1968, **218**, 929–932.
6. Rawlings, N. D., Barrett, A. J. and Bateman, A., MEROPS: the database of proteolytic enzymes, their substrates and inhibitors. *Nucl. Acids Res.*, 2012, **40**, D343–D350.
7. Dardenne, L. E., Werneck, A. S., deOliveira Neto, M. and Bisch, P. M., Electrostatic properties in the catalytic site of papain: a possible regulatory mechanism for the reactivity of the ion pair. *Proteins*, 2003, **52**, 236–253.
8. Turk, V., Stok, V., Vasiljeva, O., Renko, M., Sun, T., Turk, B. and Turk, D., *Cysteine cathepsins*: from structure, function and regulation to new frontiers. *Biochim. Biophys. Acta*, 2012, **1824**, 68–88.
9. Wiederanders, B., Kaulmann, G. and Schilling, K., Functions of propeptide parts in cysteine proteases. *Curr. Protein Pept. Sci.*, 2003, **4**, 309–326.
10. Khan, A. R. and James, M. N. G., Molecular mechanisms for the conversion of zymogens to active proteolytic enzymes. *Protein Sci.*, 1998, **7**, 815–836.
11. Cygler, M. and Mort, J. S., Proregion structure of members of the papain superfamily. Mode of inhibition of enzymatic activity. *Biochimie*, 1997, **79**, 645–652.
12. Coulombe, R., Grochulski, P., Sivaraman, J., Ménard, R., Mort, J. S. and Cygler, M., Structure of human procathepsin L reveals the molecular basis of inhibition by the prosegment. *EMBO J.*, 1996, **15**, 5492–5503.
13. Groves, M. R., Taylor, M. A., Scott, M., Cummings, N. J., Pickersgill, R. W. and Jenkins, J. A., The prosequence of procaricain forms an alpha-helical domain that prevents access to the substrate-binding cleft. *Structure*, 1996, **4**, 1193–1203.
14. LaLonde, J. M. *et al.*, The crystal structure of human procathepsin K. *Biochemistry*, 1999, **38**, 862–869.
15. Kaulmann, G., Palm, G. J., Schilling, K., Hilgenfeld, R. and Wiederanders, B., The crystal structure of a Cys25 Ala mutant of human procathepsin S elucidates enzyme prosequence interactions. *Protein Sci.*, 2006, **15**, 2619–2629.
16. Roy, S., Choudhury, D., Aich, P., Dattagupta, J. K. and Biswas, S., The structure of a thermostable mutant of pro-papain reveals its activation mechanism. *Acta Cryst. Section D., Biol. Crystallogr.*, 2012, **68**, 1591–1603.
17. Choudhury, D., Biswas, S., Roy, S. and Dattagupta, J. K., Improving thermostability of papain through structure-based protein engineering. *Protein Eng. Des. Sel.*, 2010, **23**, 457–467.
18. Roy, S., Choudhury, D., Chakrabarti, C., Biswas, S. and Dattagupta, J. K., Crystallization and preliminary X-ray diffraction studies of the precursor protein of a thermostable variant of papain. *Acta Crystallogr.*, Sect. F, 2011, **67**, 634–636.
19. Otwinowski, Z. and Minor, W., Processing of X-ray diffraction data collected in oscillation mode. *Meth. Enzymol.*, 1997, **276**, 307–326.
20. McCoy, A. J., Grosse-Kunstleve, R. W., Adams, P. D., Winn, M. D., Storoni, L. C. and Read, R. J., Phaser crystallographic software. *J. Appl. Crystallogr.*, 2007, **40**, 658–674.
21. Adams, P. D. *et al.*, PHENIX: building new software for automated crystallographic structure determination. *Acta Crystallogr.*, Sect. D, 2002, **58**, 1948–1954.

22. Emsley, P. and Cowtan, K., COOT: model-building tools for molecular graphics. *Acta Crystallogr.*, *Sect. D*, 2004, **60**, 2126–2132.

23. Murshudov, G. N., Vagin, A. A. and Dodson, E. J., Refinement of macromolecular structures by the maximum-likelihood method. *Acta. Crystallogr.*, *Sect. D*, 1997, **53**, 240–255.

24. Laskowski, R. A., MacArthur, M. W., Moss, D. S. and Thornton, J. M., PROCHECK: a program to check the stereochemical quality of protein structures. *J. Appl. Crystallogr.*, 1993, **26**, 283–291.

25. Choudhury, D., Roy, S., Chakrabarti, C., Biswas, S. and Datta-gupta, J. K., Production and recovery of recombinant propapain with high yield. *Phytochemistry*, 2009, **70**, 465–472.

26. Whitmore, L. and Wallace, B. A., DICHROWEB, an online server for protein secondary structure analyses from circular dichroism spectroscopic data. *Nucl. Acids Res*., 2004, **32**, 668–673.

27. McGrath, M. E., The lysosomal cysteine proteases. *Annu. Rev. Biophys. Biomol. Struct.*, 1999, **28**, 181–204.

28. Vernet, T. *et al.*, Processing of the papain precursor. The ionization state of a conserved amino acid motif within the Pro region participates in the regulation of intramolecular processing. *J. Biol. Chem.*, 1995, **270**, 10838–10846.

Capabilities of satellite-derived datasets to detect consecutive Indian monsoon droughts of 2014 and 2015

Satya Prakash*

Divecha Centre for Climate Change, Indian Institute of Science, Bengaluru 560 012, India

India received anomalously deficit southwest monsoon rainfall during 2014 and 2015, which resulted in consecutive droughts across the country. Reliable detection and monitoring of droughts are crucial for the reduction in drought vulnerability and associated socio-economic impacts. In this study, the potential of multiple high-resolution satellite datasets is examined using distinct drought indices over India for these two successive monsoon seasons. The satellite-derived precipitation, soil moisture and land surface temperature estimates are capable of depicting the anomalous drought conditions with some exceptions. A non-parametric multivariate standardized drought index, based on precipitation and soil moisture estimates is proven to be better in the detection of droughts when compared to conventional standardized drought indices. Overall, remote sensing satellite datasets provide immense opportunity to detect and monitor different kinds of droughts using a composite of indices. However, limited temporal records of these high-resolution satellite datasets restrain their applicability from the climatological perspective.

Keywords: Drought, multi-satellite product, non-parametric multivariate drought index, Southwest monsoon.

DROUGHT is one of the inevitable and recurring natural hazards, having paramount socio-economic impacts. The regional variability of global hydrological cycle often leads to this devastating phenomenon. Historical observations and model simulations suggested a high risk of global drought and its patterns in the twenty-first century[1–6]. Droughts are generally classified into four categories – (a) meteorological, (b) agricultural, (c) hydrological and (d) socio-economic droughts. Among these, meteorological and agricultural droughts due to deficit in precipitation and soil moisture respectively, are crucial in the Indian perspective. Indian economy is largely dependent on the agriculture sector, and the southwest monsoon rainfall spanning from June to September (JJAS) plays a vital role in agricultural production. Hence, droughts associated with the interannual variations of southwest monsoon rainfall across India have crucial impacts[7–9].

The India Meteorological Department (IMD) using gauge observations, provides weekly, monthly, and seasonal rainfall and their departures from respective climatological normal at meteorological sub-divisions and district levels over India for the southwest monsoon season. In addition, IMD uses standardized precipitation index (SPI) method at monthly gauge-based rainfall data for meteorological drought monitoring and also uses an aridity index based on a climatic water balance technique to monitor drought severity[9,10]. Although rainfall is a crucial variable responsible for drought occurrence, other variables such as soil moisture, temperature, evaporation, terrestrial water storage, etc. should also be considered along with rainfall to effectively characterize the different aspects of drought and its associated impacts. Ground-based observations of these variables are not homogenous across the country and consequently they are not sufficient enough to monitor various aspects of drought. A constellation of the Earth-observation satellites provides reasonable precipitation, soil moisture, temperature, and vegetation estimates at regular spatio-temporal intervals[11,12]. However,

*e-mail: satyaprakash@iisc.ac.in